Materials Research Bulletin 162 (2023) 112169

Contents lists available at ScienceDirect

Materials Research Bulletin

journal homepage: www.elsevier.com/locate/matresbu

Research Papers

Magnetoelectric coupling at room temperature in $LaTiO_3$/$SrTiO_3$ heterojunctions

A.Z. Simoes [a], P.P. Ortega [a], M.A. Ramirez [a], H. Moreno [a,*], C.M. Aldao [b], M.A. Ponce [c,d], F. Moura [d]

[a] School of Engineering and Sciences, São Paulo State University (UNESP), Guaratinguetá, Av. Dr. Ariberto Pereira da Cunha 333, Portal das Colinas, Guaratinguetá, SP 12516-410, Brazil
[b] Institute of Scientific and Technological Research in Electronics (ICYTE), University of Mar del Plata (UNMdP) and National Research Council (CONICET), Juan B. Justo 4302, Mar del Plata B7608FDQ, Argentina
[c] Institute of Materials Science and Technology Research (INTEMA), University of Mar del Plata (UNMdP), and National Research Council (CONICET), Juan B. Justo 4302, Mar del Plata 7600, Argentina
[d] Advanced Materials Interdisciplinary Laboratory, Federal University of Itajuba, UNIFEI – Campus Itabira, MG, Brazil

ARTICLE INFO

Keywords:
Mott insulator
Multiferroic
Thin films
Chemical synthesis

ABSTRACT

This work focuses on $LaTiO_3$ (LTO) thin films synthesized by the polymeric precursor method and deposited onto $SrTiO_3$ (STO) substrates via spin coating. The results show interesting coexisting ferromagnetic (M_r≈2.85 emu/g) - ferroelectric (P_r≈18.5 μC/cm^2) responses at room temperature. Magnetoelectric coupling can be observed under DC bias magnetic field (14 V/cm.Oe), and its dielectric constant is affected by the coupling between magnetic and electric dipoles at room temperature as well as oxygen octahedra distortion along direction *a*. Little film-substrate mismatch significantly influences the system dielectric properties. Our results suggest the possibility to induce ferromagnetic/ferroelectric phases in the LTO/STO heterojunctions using an electric/magnetic field, respectively, due to the magnetoelectric coupling. This study also helps comprehend oxygen vacancy dynamics when applying a tensile strain or an external electric field, which is fundamental for actuators, switches, magnetic field sensors, and new types of electronic memory devices.

1. Introduction

Metal oxide heterostructures (MOH) have been extensively studied over the last couple of decades due to their potential application as ferroelectric nonvolatile memories (FeRAM) and conventional volatile DRAM storage, consistently with the trend towards optoelectronics miniaturization [1–3]. ABO_3 perovskite heterojunctions composed of ABO_3 perovskites enabled the possibility of tuning electrical properties based on some unique interfacial effects (*e.g.,* interfacial metallic conductivity, superconductivity, etc.) [4–9]. Technological applications arise from their physicochemical properties/stability. Ohtomo et al. [9] used atomic-resolution electron-energy loss spectroscopy to study one to two layers of the Mott insulator lanthanum titanate ($LaTiO_3$, or LTO) embedded in the band insulator strontium titanate ($SrTiO_3$, or STO). The authors verified that instead of being confined within the LTO layer, Ti *3d* electrons are spread over STO layers (~2.5 atomic layers), and no evidence of room-temperature magnetoelectric (ME) coupling was reported.

Ferroelectricity and ferromagnetism are antagonistic properties determined by d^0-state configuration in titanates (*e.g.*, Ti^{4+}) [10]. A single-phase, room-temperature ferromagnet with a ferroelectric response is yet to be found. Thus, scientists have explored alternatives to promote simultaneous room-temperature ferroelectric-ferromagnetic responses, such as heterostructures/heterojunctions, to produce the so-called ME coupling. LTO exhibits a d^1 electronic configuration, generating an antiferromagnetic response below T_N≈140 K [11]. STO, on the other hand, displays d° configuration (*i.e.,* empty d^0 band) [12]. Ferro/magnetoelectric coupling in multiferroic materials generates electric field-controlled ferromagnetism, reduces energy consumption, and optimizes storage velocity [13]. Shao *et al.* [14] used the sol-gel route to grow (001)-oriented LTO thin films with a monoclinic perovskite structure over conducting (110)-oriented STO: Nb substrates. The authors reported ferroelectric response at the nanoscale for the films.

Researchers have long been intrigued by the possibility of obtaining

* Corresponding author.
E-mail address: hpiccolimoreno@gmail.com (H. Moreno).

https://doi.org/10.1016/j.materresbull.2023.112169
Received 13 April 2022; Received in revised form 13 October 2022; Accepted 16 January 2023
Available online 18 January 2023

50:50 ratio (ferroelectric/ferromagnetic) metal oxide heterostructures [15]. Our group has worked with synthetic routes (i.e., chemical solution deposition method) [16] to synthesize multiferroic composites. Deus et al. [16] synthesized polycrystalline $LaFeO_3$-$BiFeO_3$ (LFO-BFO) films. The authors obtained LFO-BFO multilayered microstructure and magnetic response: $P_r \approx 53$ μC/cm^2, $M_r \approx 4.6$ emu/g, $2H_c \approx 250$ G. LFO produced significant leakage current density decrease ($\sim 10^{-6}$ A/cm^2), which may be associated with large grain boundary/low oxygen vacancy densities, and the presence of cationic-related defects. However, no signal of room-temperature ME coupling was detected, which suggests that, for ABO_3-based materials, layer stoichiometry/structure, and interface are key aspects of developing nanoelectronic devices.

$LaTiO_3$ is a perovskite-structure material whose phase diagram has been widely investigated as a function of oxygen doping ($LaTiO_{3+x}$, $0<x<0.5$) [17]. Depending on oxygen content (x), LTO may present different behavior at room temperature, such as metallic, semiconductor, or ferroelectric. $SrTiO_3$, on the other hand, is a typical perovskite-like structure with cubic symmetry. STO-based heterostructures/heterojunctions exhibit extraordinary properties, which arise from their specific charge-carrier density, spin, orbital, and lattice degrees of freedom. Interactions (or coupling) between various degrees of freedom and oxygen vacancies lead to substantial changes in structural, electronic, and magnetic properties in the presence of external stimuli [18]. Researchers have employed different synthesis routes as a strategy to obtain specific heterojunction-related properties, such as spray pyrolysis [19], metal-organic deposition combined with spin coating [20], pulsed laser ablation [9], sol-gel [21], and polymeric precursor [22], etc. The polymeric precursor is a cost-effective, low-temperature method that allows using water-based solutions and enables fine stoichiometric control over the system [23].

In this work, LTO films synthesized via the polymeric precursor method were deposited onto (100)-STO substrates using spin coating to produce LTO/STO heterojunctions. (Micro)structure and ferroelectric-magnetic coupling of the heterojunctions were evaluated and interpreted in terms of point defects (e.g., oxygen vacancies and cationic defects). Our results show the possibility of producing ferromagnetic/ferroelectric phases heterojunctions induced by an external electric/magnetic field, respectively, which is a result of the magnetoelectric coupling effect. This phenomenon helps us comprehend the oxygen vacancy density role when applying a tensile strain or an external electric field, which is fundamental for magnetic field sensors, switches, actuators, and new types of electronic memory devices.

2. Experimental procedure

2.1. LTO/STO film preparation

In order to carry out electrical measurements at the substrate/film interface, LTO/STO films were built, as reported in previous works [24]. Then, the $LaTiO_3$ (LTO) precursor solution was prepared mixing lanthanum (III) nitrate hexahydrate (Sigma-Aldrich, 99.9%), titanium (IV) isopropoxide (Sigma-Aldrich, 99.9%), citric acid (Sigma-Aldrich, 99.0%), and ethylene glycol (Sigma-Aldrich, 99.9%) at a 1: 4: 16 M proportion of metal to citric acid to ethylene glycol. Later, LTO films synthesized via the polymeric precursor method were deposited onto (100)-STO substrates using spin coating to produce LTO/STO heterojunctions. To do so, the LTO precursor solution was spread over a standard size (*width* = 0.5 cm, *length* = 1.0 cm, *thickness* = 0.5 mm) (100)-$SrTiO_3$ monocrystalline substrate (speed = 5000 rpm; time = 30 s). The LTO films were obtained after the coated substrate was heat-treated at 400 °C for 2 h to eliminate the organic material. This process was repeated 2 times to obtain 50 nm thick films. Finally, conventional electrodes were used to generate 10 μm-wide Ti/Au alloy parallel bars as active regions. Then, a focused ion beam (FIB) microscope was used to expose these active regions accordingly. Pt injected was used as electrodes [24].

Three films were prepared for the test devices. The polar properties of the heterojunction were measured in the center film to guarantee reproducibility and repeatability of the obtained properties. Three samples were prepared: sample 1 was used for XRD, AFM, and STEM analyses, while samples 2 and 3 were reserved for electrical measurements. The *P-E, I-V*, and magnetoelectric coefficient vs. DC bias magnetic field curves were measured at room temperature (sample 2) while the *M-H* and dielectric curves were recorded as a function of the temperature (sample 3). Based on thermal analysis data (not shown here) the films were heated to 800 °C for 2 min in a rapid thermal annealing (RTA) furnace (~150 °C/s) under nitrogen (1 mL/min) atmosphere. This temperature guarantees all organic material is decomposed and the crystalline film could be obtained [25]. Thermal treatment under nitrogen atmosphere was conducted to avoid pyrochlore structure formation.

2.2. Characterization

2.2.1. (Micro)structural characterization

X-ray diffraction (XRD) was carried out on a Rigaku diffractometer (Rint 2000) using Cu-K_α radiation over the $20^\circ \leq 2\theta \leq 60^\circ$ range. Quantitative phase analysis of the films was performed using the *Rietveld* method [26] on Topas V5 [27]. The surface morphology of the films was evaluated using an atomic force microscope (Digital Instruments, Nanoscope IV controller) operating under tapping mode. Piezoelectric micrograph images were also acquired on an atomic force microscope (Digital Instruments, Multimode Scanning Probe Microscope with Nanoscope IV controller). Micrograph images were collected over 5×5 μm and 3×3 μm areas applying −12 V/+12 V, respectively, using a conductive PFM tip. Transmission Electron Microscopy (TEM) was performed on a Phillips (CM 200 Microscope) at a 200 kV accelerating voltage to investigate LTO/STO heterojunction local composition/structure.

2.2.2. Electrical and ferroelectric response

Film hysteresis behavior was evaluated at 60 Hz using a magnetometer (Radiant Technology, RT6000HVS). Impedance spectroscopy measurements were performed using a frequency response analyzer (HP 4192) with an amplitude of 100 mV. Finally, a four-probe technique (PC-controlled four-probe direct current (DC)) was used to carry out resistivity measurements over the 0.01 Hz$\leq f \leq$10 MHz.

2.2.3. Magnetic and multiferroic response

Magnetoelectric signals were measured using a lock-in amplifier (EG&G model 5210) set up with low capacitance (25 pF) and high resistance (100 MΩ), and AC-magnetic field (*B*) up to 10 Oe (*f*=7 kHz) superimposed to the DC-field. A Helmholtz-type coil (180 turns; 50 mm in diameter) was used to produce the AC-field, driven by an AC-current generated by a function generator (Philips PM5192). The AC-field amplitude was calculated based on the driving current, measured using a multimeter (Keithley 196, System DMM). Longitudinal and transverse magnetic field measurements were carried out on an electromagnet Cenco Instruments (J type), used to produce the DC-magnetic bias field. Time-varying DC-field was obtained by a programmable DC power supply (Phillips PM2810 60 V/5 A/60 W). DC-magnetic field was measured using a Hall probe. Finally, magnetization measurements were performed using a Quantum Design™ vibrating-sample magnetometer (VSM).

3. Results and discussion

3.1. (Micro)structural characterization

Fig. 1 exhibits diffractograms of 50 nm thick (2 layers) LTO thin films crystallized under an nitrogen atmosphere in an RTA furnace. It reveals diffraction peaks at $2\theta \approx 32.75$, 34.88, and 39.10° associated with an

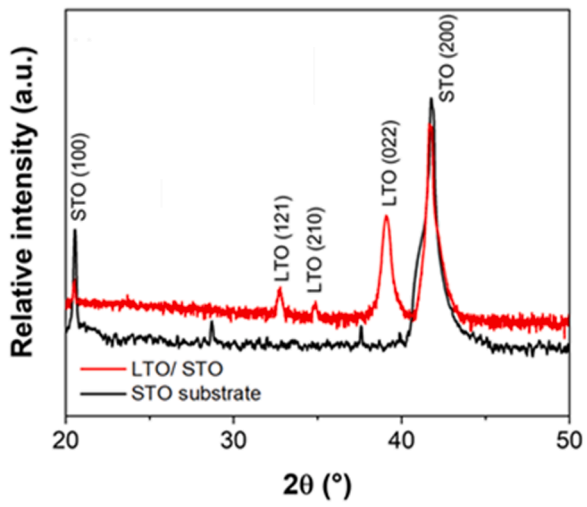

Fig. 1. (a) X-ray diffraction of the LTO/STO film crystallized at RTA at 800 °C for 2 min followed by thermal treatment at N_2 atmosphere.

orthorhombic $LaTiO_3$ structure (mp-#22,013) *Pbnm* space group). (100)-STO substrate exhibits a cubic structure (mp-#5229) (*P1*) with a characteristic peak at 2θ≈42°. No traces of pyrochlore $La_2Ti_2O_7$ peaks were identified, which indicates nitrogen promotes ordering of the oxygen planes leading to *Pbnm*-orthorhombic phase formation [28]. The peak associated with the (200) plane in the $SrTiO_3$ substrate slightly shifts towards lower 2θ angles, suggesting LTO/STO formation may lead to a structural mismatch.

Fig. 2(a) presents LTO/STO heterojunction surface analysis using atomic force microscopy (AFM), which exhibits R_{ms}≈0.584 nm. Additionally, the mean grain size (~25 nm) was measured, and the grain size distribution curve was determined, indicating the presence of small grains with distinguishable grain boundaries, implying a pseudo-2D growth mode (*Stranski–Krastanov*) [29]. Released literature relates low roughness films (R_{ms} < 1.0 nm) to atomically smooth surfaces grown by a layer-by-layer mechanism [30]. Fig. 2(b) displays a micrograph image of the LTO/STO interfaces obtained using scanning transmission electron microscopy (STEM). The TEM micrograph shows the disposition of both the LTO (≈4 nm) domain walls, which appear prominent above the STO substrate, and approximately 60° rotated counterclockwise from the STO domain walls, as highlighted in Fig. 2(b). While this is not very close to the polar axis, there should still be a measurable polarization (though lower than along the polar axis) normal to the surface. This result may be related to the lower roughness (R_{ms}) and to the absence of defined grain boundaries.

3.2. Electrical response

Fig. 3(a) shows current vs. voltage (*I-V*) measurements performed between −12 V and +12 V. The results show a typical behavior characteristic of polar interfaces. Hysteresis loop shape suggests resistance state shifts from high to low caused by a sudden current change from +5 V to −5 V, followed by a low-high resistance state shift when voltage increases from −4 V to +4 V, with an on/off ratio under +1 V (10^5). Additionally, hysteresis loop symmetry confirms that oxygen vacancies do not contribute to piezoelectric response under an applied electric field. This result is corroborated by on/off state stability with time by retention data. Time-dependent current (Fig. 3b) reveals no low/high conducting state decay after half a day. Fig. 3(b) inserts exhibit out-of-plane piezoelectric force microscopy (*PFM*) micrograph images, which indicate that polarization on LTO films can be switched between high and low domains by an external electric field of opposite signs. Both high and low domains are stable after half a day, consistently with resistance states. Fig. 3(c) displays the ferroelectric hysteresis nature at 60 Hz. Analysis indicates high remnant polarization (P_r≈18.2 μC/cm^2) and drive voltage close to 1.45 V to which a low ferroelectric loss can be associated with low applied frequency. The remnant polarization was increased compared with bulk ceramics, polycrystalline films, and *c*-axis-oriented single crystals. This result may be explained by the formation of LTO/STO heterojunctions in relation to an orthorhombic LTO structure over the cubic LTO substrate, as shown by *XRD* and *TEM* micrograph images. Furthermore, ferroelectric polarization direction along additional oxygen planes (along direction *a*) may be caused by oxygen octahedra distortion. Hence, high polarization may be a result of (500) polar axis contributions, close to the surface normal to the film. The heterojunctions are *a*-axis oriented due to an uneven oxygen ion distribution along the exposed (100)-TiO_2 planes on the STO substrates. Ferroelectric hysteresis loop shape (Fig. 3c) also confirms the observed oriented growth of ordered *a*-axis in the LTO film, indicating that oxygen ordering within planes parallel to the surface leads to lattice relaxation at interface and implying small lattice mismatch. Consequently, the symmetric loop observed reveals no traces of grain boundary/interfacial complex defect dipoles, which suggests a film free from imprinting phenomena.

Fig. 4(a–c) exhibits the impedance spectroscopy (IS) curves obtained over a 10^{-2}–10^6 Hz frequency range, at 423 and 473 K. Results in Fig. 4 (a) indicate a smaller circumference for higher temperatures, suggesting grain boundary resistance (R_{gb}) decreases with temperature, which is expected since temperature facilitates current transport mechanisms [31,32]. Film shape does not enable simple representation of the observed electrical response in the form of RC-circuits, indicating the need for a more refined electrical circuit model [33]. In previous work, it was shown that simple circuits may not always be adequate to practically represent impedance vs. frequency responses [34]. Fig. 4(b-c) display the parallel electrical capacitance (C_p) and resistance (R_p), respectively, as a function of frequency at 423 K and 473 K. C_p increases at low frequencies as a result of the LTO/STO interface and, possibly, due to deep bulk traps at higher temperature (473 K). It has been previously proposed that the electrical behavior of a film at low frequencies can be better described by an electrical model such as the one shown in Fig. 4(b), which for simplicity neglects bulk resistance (R_b). In this circuit, resistance R_t and capacitance C_t mimic deep trap effects [35].

Fig. 4(d) shows equivalent circuits considering: (I) overall LTO/STO system impedance contributions; and (II) the equivalent elements in the LTO/STO heterojunction – interface electrode, grain boundary, and bulk. An R_t element has also been included to account for deep bulk traps in the system, which are connected to constant phase elements (*CPEs*) in series but do not necessarily appear in the overall equivalent circuit model. Regularly, in a semiconductor polycrystal, the impedance is dominated by grain boundary and can be described as an RC-circuit. Thus, impedance (Z_{gb}) can be calculated based on grain boundary resistance (R_{gb}) and capacitance (C_{gb}) values in parallel, as given in Eq. (1).

$$Z_{gb} = \frac{R_{gb}\frac{1}{j\omega C}}{R_{gb} + \frac{1}{j\omega C}} \tag{1}$$

that can also be expressed in the form of Eq. (2)

$$Z_{gb} = \frac{R_{gb} - j\omega R_{gb}^2}{1 + \omega^2 + R_{gb}^2 C^2} \tag{2}$$

Eq. (3) represents Eq. (2) considering its real and imaginary parts,

$$Z_{gb}^{'2} + Z_{gb}^{''2} = R_{gb} Z_{gb}^{'} \tag{3}$$

where $Z_{gb}^{'}$ and $Z_{gb}^{''}$ correspond to grain boundary impedance, real and imaginary parts, respectively. Then, rewriting Eq. (3) in the form of a circumference function of radius $R_{gb}/2$ centered at $R_{gb}/2$, we obtain Eq. (4):

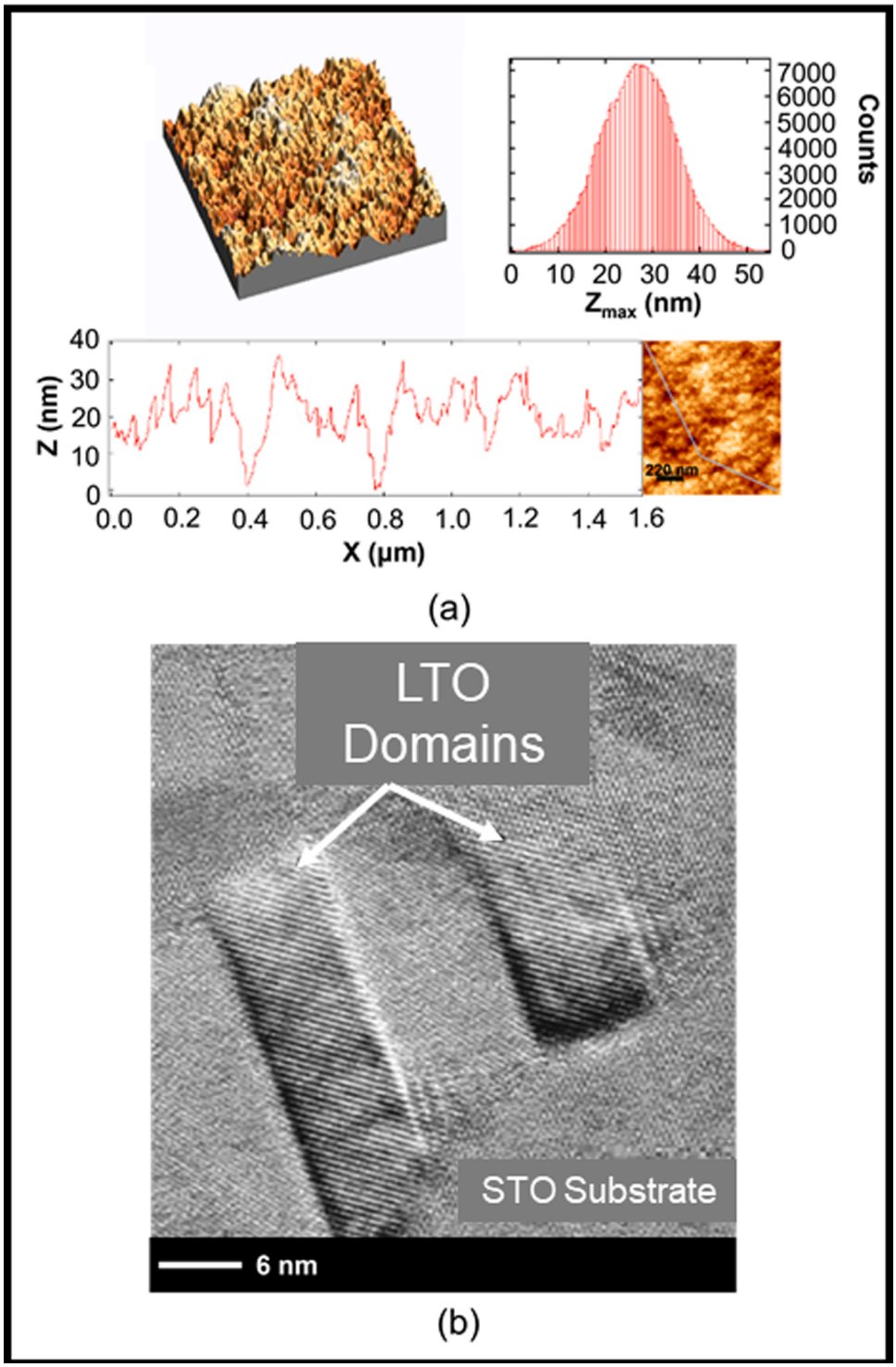

Fig. 2. (a) Atomic force microscopy image of the LTO/STO film and (b) Scanning transmission electron microscopy (STEM) image of the LTO/STO heterojunction crystallized at RTA at 800 °C for 2 min followed by thermal treatment at N_2 atmosphere.

$$\left(\frac{Z'_{gb} - R_{gb}}{2}\right)^2 + Z''^2_{gb} = \left(\frac{R_{gb}}{2}\right)^2 \quad (4)$$

Adding bulk resistance, R_b, the impedance semicircle is shifted to the right. Thus, both R_b and R_{gb} can be determined from low- and high-frequency resistances, while C_{gb} is related to the maximum reactance values. Fig. 4 (d-I) represents an equivalent electrical circuit [36]. To represent the actual electrical behavior of the LTO/STO – interface system, we must include the following parameters related with the different components: (1) R_{LTO}: LTO electrical resistance; (2) C_{LTO}: LTO electrical capacitance; (3) R_{INT}: LTO/STO interface electrical resistance; (4) C_{INT}: LTO/STO interface electrical capacitance; and (5) R_{STO}: STO electrical resistance. Considering that $wC_{LTO} << 1/R_{INT}$ and $1/R_{STO} >> wC_{INT}$, the equivalent circuit can be simplified to the circuit shown in Fig. 4(d-II) for the frequency range. The STO dielectric permittivity can reach values as high as 1.8×10^4 [37–39], while LTO intrinsic dielectric constant ($\varepsilon_\infty \approx 20 \pm 2$ for $E \perp a$; $\varepsilon_\infty \approx 44 \pm 2$ for $E \,||\, a$ at lower temperatures) [40]. From IS results and considering Eq. (5-7) we

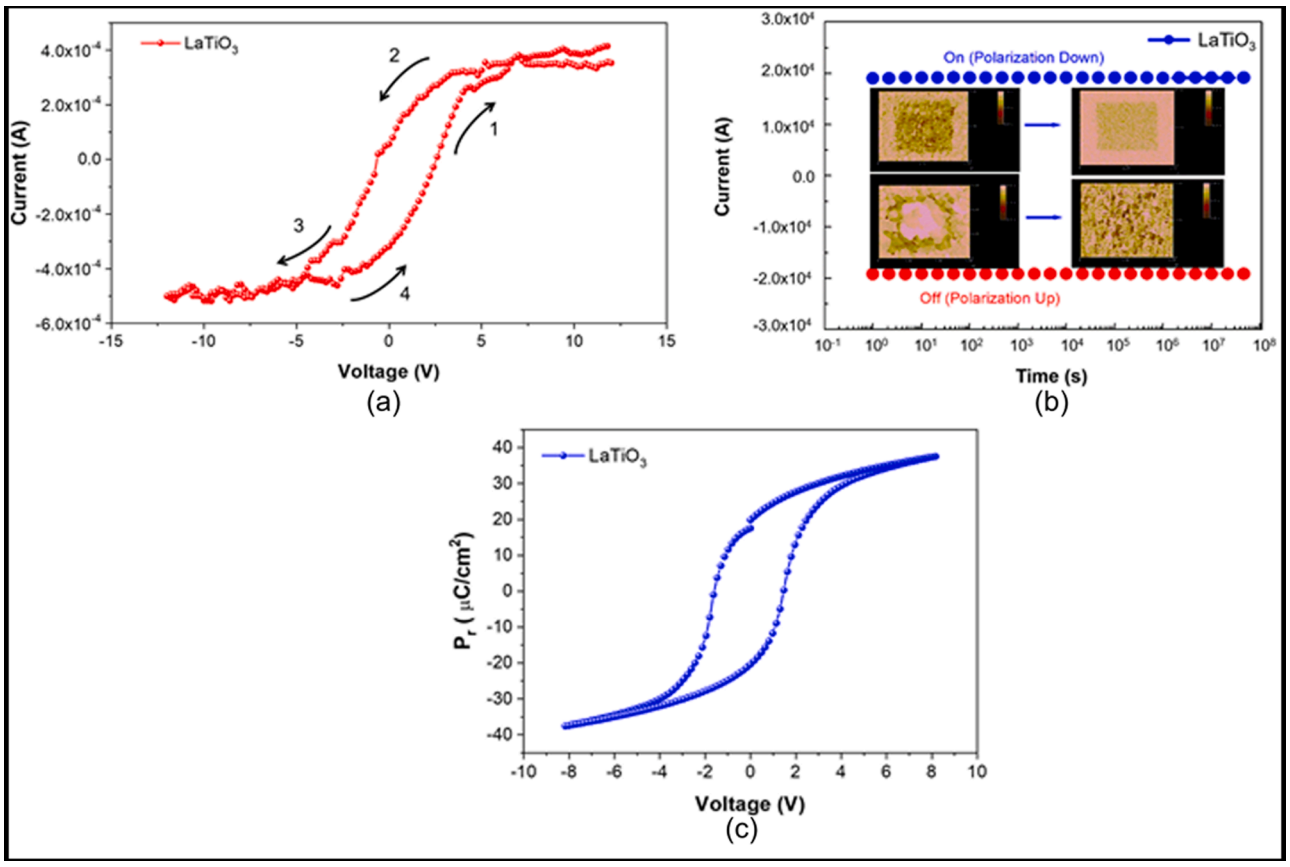

Fig. 3. (a) Current versus voltage (b) Current versus time (c) Ferroelectric loop of the LTO/STO heterojunction.

deduce the capacitance of the LTO film is much smaller (6.6×10^{-3} pF) than the measured value (12 pF) [37].

$$\frac{D}{e} = 200 \gg 1 \rightarrow C_{(LTO)} \cong \frac{\varepsilon_0 \varepsilon_r Z}{\frac{D}{e_{(LTO)}} + 0.8825} \tag{5}$$

$$C_{LTO} \cong \varepsilon_r x 2.2 x 10^{-16} F \tag{6}$$

$$\text{For } \varepsilon_r \cong 30 \rightarrow C_{LTO} \cong 6.6 x 10^{-16} F = 0.0066 pF \tag{7}$$

Hence, film (LTO) capacitance becomes negligible compared to substrate (STO) in the heterojunction due to its thickness, and we estimated the capacitance based on the STO substrate alone (Fig. 4e), considering Eq. (8),

$$C_{STO} = \frac{\varepsilon_0 \varepsilon_r Z}{\pi} \left[\sin^{-1} \left(\frac{2e_{(STO)}}{D} \right) + 0.234 \right] \tag{8}$$

where $\frac{2e}{D} = 100$, $C_{STO} = \varepsilon_r x 7.8 x 10^{-14}$ F for a measured capacitance of about 12 pF, and $\varepsilon_{\text{rsubstrate}} \approx 154$.

STO intrinsic dielectric constant was found to be $\varepsilon_r \approx 154$, which can be considered high compared to conventional semiconductors. In our frequency region, electrodes effects, dipoles and charge transport no longer contribute to ε and its value can be determined by the ionic and electronic effects [41]. The dielectric permittivity value may be related to structural distortions in TiO_6 octahedra along the *a*-axis leading to ferrodistortive orbital order as a result of higher polarizability in the basal plane. Thus, a higher polarization of the deformed octahedra along the *a*-axis is expected. X-value on partially filled *D*-shell compounds (*e.g.,* $LaTiO_{3+x}$), in which Ti^{3+}: d^1 may behave as metals, semiconductors, or ferroelectrics at room temperature. Furthermore, for low oxygen contents ($0.0 < x < 0.2$) crystal structure consists of three-dimensional [TiO_6] octahedra networks [42] in which partially filled *d*-orbitals hamper strong static/dynamic ionic polarization effects drive polar order. Hence, in $LaTiO_3$ structures, orbital occupancy/order must be considered due to their strong correlation to anisotropy and polarization effects. Therefore, our results suggest that the band configuration within the film is strongly influenced by lattice relaxation at the interface, leading to the dielectric properties of the Mott insulator $LaTiO_3$. In this context, it appears that the LTO/STO interface behaves as an independent system with unique physicochemical properties.

3.3. Magnetic response

Fig. 5(a) shows magnetization curves as a function of the applied magnetic field and temperature. Results indicate weak ferromagnetic behavior of the heterojunctions at all considered temperatures investigated, in agreement with Sun *et al.* [43], who reported weak ferromagnetic behavior of $La_2Ti_2O_7$ perovskite nanocrystals at room temperature due to the presence of superficial oxygen vacancies. Ferromagnetic response decreases with structural defect concentration (e.g., oxygen vacancies, etc.) at the grain surface. Thus, the weak ferromagnetism of our heterojunction may also originate from oxygen non-stoichiometry, leading to Ti electrons occupying the e_g orbital, which become spin-polarized. Fig 5(a) insert reveals significant remnant magnetization (M_r) increase during cooling along with coercive field (H_c) decrease during heating. The lack of magnetic saturation may be explained by intrinsic magnetic states located at the interface (Ti^{3+} moments). Simultaneously, charge carriers (i.e., electrons and holes) move through these interfaces, whose defects contribute to charge trapping among clusters. Fig. 5(b) exhibits the magnetoelectric coefficient vs. DC bias magnetic field curves, which enables the evaluation of the ferroelectric-magnetic coupling behavior in the longitudinal direction. The obtained heterojunctions are formed by individual layers in which ferroelectric-magnetic properties are retained while originating a

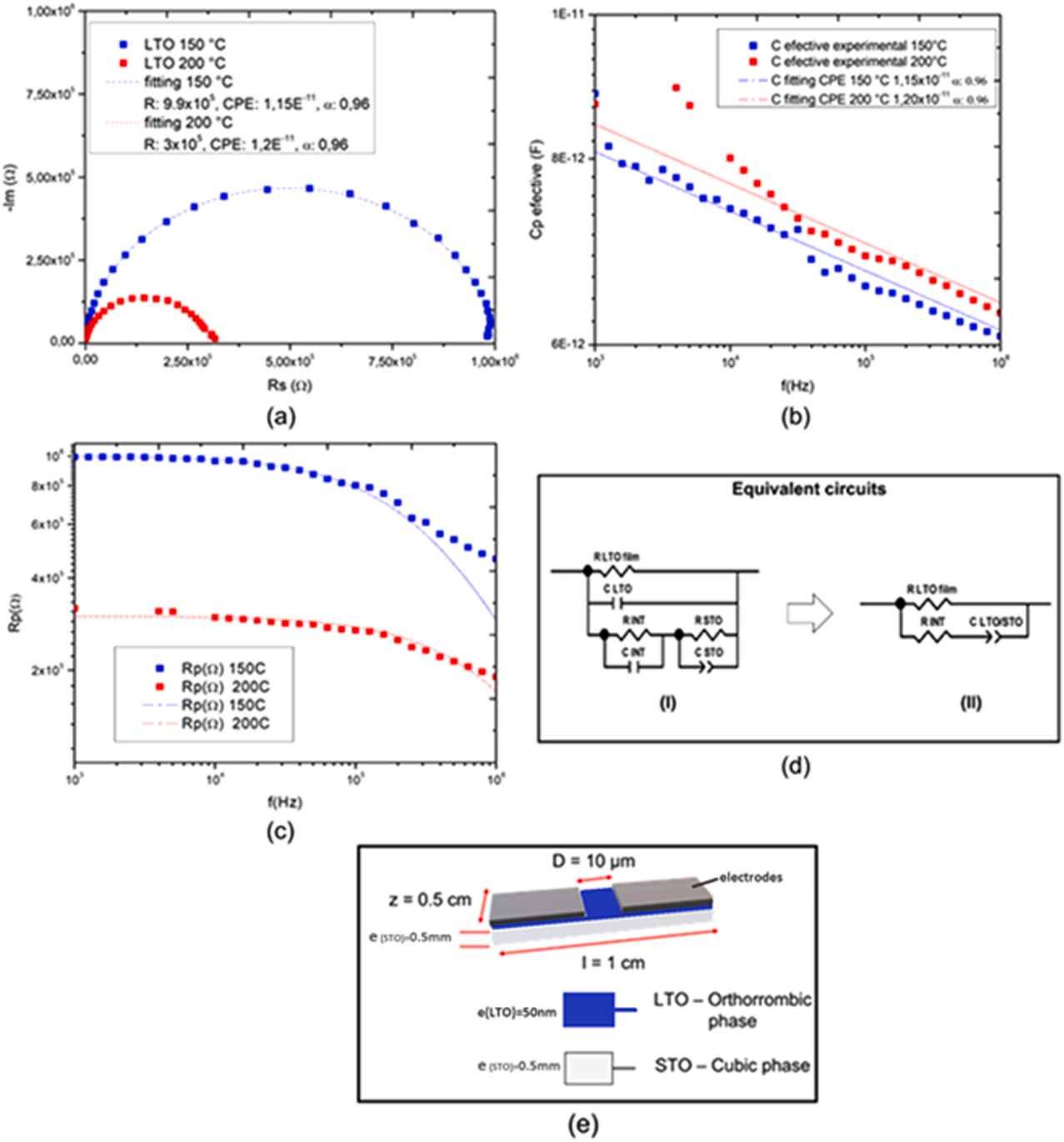

Fig. 4. (a) Cole-Cole plot of the complex-impedance diagram in the temperature range 423 K and 473 K (b) Total electrical capacitance, (c) Total parallel resistance dependence with frequency and (d) equivalent circuit of the LTO/STO heterojunction at different temperatures and (e) Geometrical configuration of coplanar band electrodes of the LTO/STO heterojunction crystallized at RTA at 800 °C for 2 min followed by thermal treatment at N_2 atmosphere and Geometrical configuration of the $SrTiO_3$ substrate.

magnetoelectric coupling response. Structural match allows coherent growth with atomically flat interfaces (Fig. 2b), which is a prerequisite for studying magnetoelectric coupling and other interface-related effects. However, special attention must be given to prevent interdiffusion at interfaces, such as cation intermixing. The magnetoelectric coefficient measured in the longitudinal direction was found to be ≈14 V/cm.Oe, which can unveil similar crystal structure distortion between LTO and STO forming the heterojunction, which is compatible with coupling of lattice modes. Compared to other perovskite materials based on heterostructured thin films of lanthanum ferrite ($LaFeO_3$) and bismuth ferrite ($BiFeO_3$) the magnetoelectric coefficient as a function of the polarization magnetic field in longitudinal and transversal directions reveals hysteretic behavior for the 6-LFO/4-BFO heterostructured film with observed magnetoelectric coefficient of 12 V/cmOe in the longitudinal direction and 3 V/cmOe in the transversal direction. The authors mentioned that the higher values of the magnetoelectric coefficient compared to pure BFO thin films in the longitudinal direction is a consequence of the antiferromagnetic axis of the artificial heterostructure which under stress can suppress the spiral spin structure [22].

The electromagnetic properties of the heterojunction might be due to hopping conduction mechanisms, which can be influenced by MO_6 octahedra distortions within its structure. On crystalline films, lower

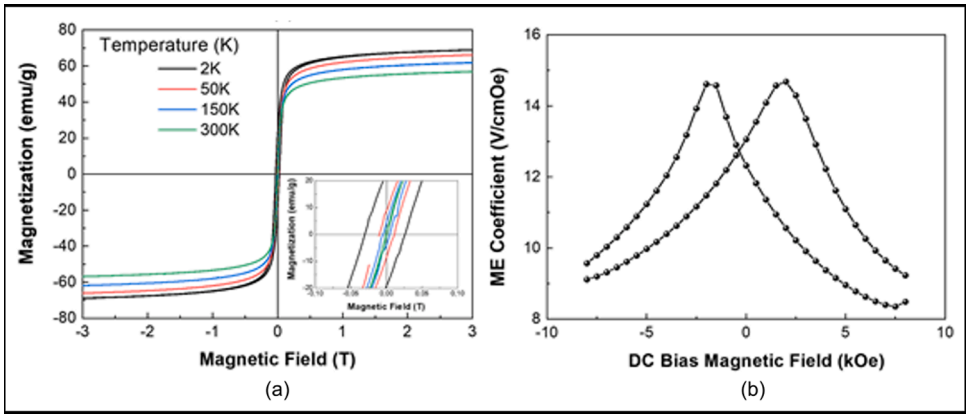

Fig. 5. (a) Magnetic data as a function of temperature and (b) Magnetoelectric signal of the LTO/STO heterojunction crystallized at RTA at 800 °C for 2 min followed by thermal treatment at N_2 atmosphere.

oxygen vacancy density may be associated with the surface of a semiconductor with high surface-to-volume ratio. Hence, the presence of two different Ti clusters ([TiO_6] and [TiO_5. V_O]) leads to lower film conductivity since oxygen vacancies induce new energy levels within the bandgap region. Positively charged oxygen vacancies induce electron-hole polaron (*Jahn-Teller* bipolarons) formation around them, establishing charge transfer from [TiO_6] and [TiO_5. V_O] clusters [44]. A possible source for the magnetocoupling effect is Ti-O-Ti bond length/angle changes as a result of tilting/rotation in oxygen octahedra, which influences ferroelectric and magnetic responses. The distorted [TiO_6] octahedral sites are defined by their rotations towards cubic [LaO_8] clusters within the $LaTiO_3$ lattice, described by their tilt angle. Lattice distortions created by the nitrogen atmosphere and [TiO_6] tilting, produce a local electric field, generating ferroelectric ordering in the Mott insulator LTO. Moreover, oxygen rotation at both sites is typical of antiferromagnetic distorted perovskites and coupling between antiferromagnetic order and tilt angle (also known as rotomagnetic coupling) is essential to explain its properties.

To deeply understand such phenomenon, the co-exposed surfaces at the interfaces formed by LTO/STO heterojunction should be studied using an explicit atomistic interface model via density functional theory (DFT). The interface nature can be tailored by looking at the structure, electronic properties, and band edges of the separate units, allowing them to get a deep insight into the polar behavior of such interfaces.

4. Conclusions

In this work, $LaTiO_3$ (LTO) thin films synthesized via the polymeric precursor method were spread over $SrTiO_3$ (STO) using spin coating to obtain LTO/STO heterojunctions. (Micro)structural, electronic, ferroelectric, and magnetic properties of the LTO/STO heterojunction and its interface were evaluated considering the following aspects: oxygen vacancies; structural deformations (including cationic disorder); and electronic interface. This research reveals the importance of oxygen defects at the interface and surface of LTO/STO heterojunctions. The obtained heterojunctions exhibited room-temperature coexisting ferromagnetic (Mr≈2.85 emu/g) and ferroelectric (Pr≈18.5 μC/cm^2) response, owing to its ferromagnetic coupling behaviors under DC bias magnetic field 14 V/cm.Oe. Magnetoelectric coupling at LTO/STO heterojunctions might be a result of the influence of the magnetic field over the ferroelectric domains due to coupling between ferroelectric and ferromagnetic domains. The little mismatch between film and substrate significantly influences LTO/STO heterojunctions dielectric properties. From complex IS data, we proposed that the capacitance is governed by the STO substrate, and the resistance is controlled by the LTO film. LTO intrinsic dielectric constant (ε_r≈30) can be mostly associated with ionic and electronic polarization. Our results show the possibility of inducing ferromagnetic/ferroelectric phases in LTO/STO heterojunctions by applying an electric/magnetic field, respectively, due to its ME coupling. Also, our study helps comprehend oxygen vacancy dynamics under tensile strain/external electric field, which is fundamental for actuators, switches, magnetic field sensors and new types of electronic memory devices.

CRediT authorship contribution statement

A.Z. Simoes: Writing – original draft, Investigation. **P.P. Ortega:** Formal analysis, Writing – review & editing. **M.A. Ramirez:** Formal analysis, Visualization. **H. Moreno:** Formal analysis, Visualization. **C.M. Aldao:** Formal analysis, Writing – review & editing. **M.A. Ponce:** Writing – original draft, Formal analysis, Investigation. **F. Moura:** Conceptualization, Supervision.

Declaration of Competing Interest

The authors declare that they have no known competing financial interests or personal relationships that could have appeared to influence the work reported in this paper.

Data availability

Data will be made available on request.

Acknowledgments

The authors thank the São Paulo Research Foundation (FAPESP) under CEPID/CDMF grants (#2013/07296–2, #2019/07413–5, and #2018/18236-4 for their financial support.

References

[1] S. Zhang, et al., Two-dimensional heterostructures and their device applications: progress, challenges and opportunities—review, J. Phys. D. Appl. Phys. 54 (2021), 433001.
[2] J.M. Hu, L.Q. Chen, C.W. Nan, Multiferroic heterostructures integrating ferroelectric and magnetic materials, Adv. Mater. 28 (2016) 15–39.
[3] A. Lahgere, M.J. Kumar, 1-T capacitorless DRAM using laterally bandgap engineered Si-Si:c heterostructure bipolar I-MOS for improved sensing margin and retention time, IEEE Trans. Nanotechnol. 17 (2018) 543–551.
[4] S. Thiel, et al., Tunable quasi-two-dimensional electron gases in oxide heterostructures, Science 313 (2006) 1942–1945.
[5] M. Huijben, et al., Defect engineering in oxide heterostructures by enhanced oxygen surface exchange, Adv. Funct. Mater. 23 (2013) 5240–5248.
[6] H. Hilgenkamp, Novel transport phenomena at complex oxide interfaces, Mater. Res. Bull. 38 (2013) 1026–1031.
[7] M.B Shalom, et al., Shubnikov-de Haas oscillations in $SrTiO_3/LaAlO_3$ interface, Phys. Rev. Lett. 105 (2010), 206401.

[8] P. Moetakef, et al., Toward an artificial Mott insulator: correlations in confined high-density electron liquids in $SrTiO_3$, Phys. Rev. B - Condens. Matter. Phys 86 (2012), 201102.

[9] A. Ohtomo, et al., Artificial charge-modulationin atomic-scale perovskite titanate superlattices, Nature 419 (2002) 378–380.

[10] T. Shimada, Y. Uratani, T. Kitamura, Vacancy-driven ferromagnetism in ferroelectric $PbTiO_3$, Appl. Phys. Lett. 100 (2012), 162901.

[11] Y. Tokura, Fillingness dependence of electronic structures in strongly correlated electron systems: titanates and vanadates, J. Phys. Chem. Solids 53 (1992) 1619–1625.

[12] K. Maekawa, et al., Photoemission study of TiO_2/VO_2 interfaces, Phys. Rev. B - Condens. Matter. Phys. 76 (2007), 115121.

[13] W. Eerenstein, N.D. Mathur, J.F. Scott, Multiferroic and magnetoelectric materials, Nature 442 (2006) 759–765.

[14] Z. Shao, et al., Microstructure and nanoscale piezoelectric/ferroelectric properties in $La_2Ti_2O_7$ thin films grown on (110)-Oriented doped Nb:$srTiO_3$ substrates, Adv. Eng. Mater. 13 (2011) 961–969.

[15] N.A. Hill, Why are there so few magnetic ferroelectrics? J. Phys. Chem. B. 104 (2000) 6694–6709.

[16] R.C. Deus, et al., Magnetocoupling and domain structure of $BiFeO_3/LaFeO_3$ heterostructures deposited on $LaSrCoO_3/Pt/TiO_2/SiO_2/Si$ (100) substrates by the soft chemical method, J. Mater. Sci. Mater. Electron. 28 (2017) 8630–8642.

[17] J. Fompeyrine, J.W. Seo, J.P. Locquet, Growth and characterization of ferroelectric $LaTiO_{3-5}$ thin films, J. Eur. Ceram. Soc. 19 (1999) 1493–1496.

[18] D.V. Christensen, et al., Stimulating oxide heterostructures: a review on controlling $SrTiO_3$-based heterointerfaces with external stimuli, Adv. Mater. Interfaces. 6 (2019), 1900772.

[19] D.S. Todorovsky, et al., Deposition and characterization of $La_2Ti_2O_7$ thin films via spray pyrolysis process, Appl. Surf. Sci. 253 (2007) 4560–4565.

[20] Z. Zhao, Y. Zhang, J. Yang, H. Li, W. Song, X. Zhao, Low-temperature synthesis of $La_2Ti_2O_7$ nanocrystal by metallorganic decomposition method, J. Ceram. Soc. Japan. 113 (2005) 67–70.

[21] W.S. Kim, et al., Microstructure and electrical properties of $Ln_2Ti_2O_7$ (Ln=La, Nd), Thin Solid Films 420–421 (2002) 575–578.

[22] P.P. Ortega, L.S.R. Rocha, C.C. Silva, M. Cilense, R.A.C. Amoresi, E. Longo, A. Z. Simões, Multiferroic behavior of heterostructures composed of lanthanum and bismuth ferrite, Ceram. Int. 42 (2016) 16521–16528.

[23] R.A.C. Amoresi, et al., Electrosteric colloidal stabilization for obtaining $SrTiO_3/TiO_2$ heterojunction: microstructural evolution in the interface and photonics properties, J. Eur. Ceram. Soc. 38 (2018) 1621–1631.

[24] R.A.C. Amoresi, et al., Direct preparation of standard functional interfaces in oxide heterostructures for 2DEG analysis through beam-induced platinum contacts, Appl. Phys. Lett. 113 (2018), 131603.

[25] A.C.T. Cabral. Desenvolvimento de heteroestruturas artificiais para aplicação em memórias correlacionadas por elétrons [thesis]. Itabira: Federal University of Itajubá; 2019.

[26] H.M. Rietveld, A profile refinement method for nuclear and magnetic structures, J. Appl. Crystallogr. 2 (1969) 65–71.

[27] A.A. Coelho, TOPAS and TOPAS-Academic: an optimization program integrating computer algebra and crystallographic objects written in C++, J. Appl. Crystallogr. 51 (2018) 210–218.

[28] B. Michael Kestigian, et al., The Preparation of Lanthanum Titanium Oxide, $LaTiO_3$, J. Am. Chem. Soc. 76 (2002) 6027.

[29] J.E. Prieto, I. Markov, Stranski–Krastanov mechanism of growth and the effect of misfit sign on quantum dots nucleation, Surf. Sci. 664 (2017) 172–184.

[30] N.C. Bristowe, et al., The origin of two-dimensional electron gases at oxide interfaces: insights from theory, J. Phys. Condens. Matter. 26 (2014), 143201.

[31] G. Gong, et al., Multiferroic properties in transition metals doped $La_2Ti_2O_7$ ceramics, J. Alloys Compd. 611 (2014) 30–33.

[32] H.L. Tuller, Ionic conduction in nanocrystalline materials, Solid State Ionics 131 (2000) 143–157.

[33] Y. Taguchi, et al., Critical behavior in $LaTiO_{3+\delta/2}$ in the vicinity of antiferromagnetic instability, Phys. Rev. B 59 (1999), 7917.

[34] M.A. Ponce, et al., Effects of previous treatments on the electrical response of SnO_2-thick films exposed to a CO atmosphere, Mater. Sci. Eng. B. 123 (2005) 130–135.

[35] B.S. Chiou, M.C. Chung, Admittance spectroscopy and trapping phenomena of ZnO based varistors, J. Electron. Mater. 20 (1991) 885–890.

[36] M. Cwik, et al., Crystal and magnetic structure of $LaTiO_3$: evidence for nondegenerate t_{2g} orbitals, Phys. Rev. B. 68 (2003), 060401.

[37] D. Pascal, P. Dansas, C. Bru, S. Laval, Accurate analytical determination of the resistance of a semiconducting layer between two coplanar electrodes, Semicond. Sci. Technol. 4 (1989) 633–638.

[38] M. Gasperin, Dititanate de lanthane, Acta Cryst 31 (1975) 2129–2130.

[39] R. Viana, et al., Dielectric spectroscopy in $SrTiO_3$, Phys. Rev. B. 50 (1994) 601–604.

[40] C.R. Crowell, V.L. Rideout, Normalized thermionic-field (T-F) emission in metal-semiconductor (Schottky) barriers, Solid State Electron. 12 (1969) 89–105.

[41] P. Lunkenheimer, T. Rudolf, J. Hemberger, A. Pimenov, S. Tachos, F. Lichtenberg, A. Loidl, Dielectric properties and dynamical conductivity of $LaTiO_3$: From dc to optical frequencies, Phys. Rev. B 68 (2003) 245108–245113.

[42] K. Zou, et al., $LaTiO_3/KTaO_3$ interfaces: a new two-dimensional electron gas system, APL Mater. 3 (2015), 036104.

[43] L. Sun, J. Hu, et al., Room-temperature ferromagnetism and ferroelectricity of nanocrystalline $La_2Ti_2O_7$, J. Alloys Compd. 502 (2010) 176–179.

[44] R.A.C. Amoresi, et al., Metallic behavior in STO/LAO heterostructures with non-uniformly atomic interfaces, Mater. Today Commun. 24 (2020), 101339.